Tilt effects on moment tensor inversion in the near field of active volcanoes

M. van Driel,* J. Wassermann, C. Pelties, A. Schiemenz and H. Igel

Department of Earth and Environmental Sciences, Ludwig-Maximilians-University, Munich, Germany. E-mail: Martin@vanDriel.de

SUMMARY

Dynamic tilts (rotational motion around horizontal axes) change the projection of local gravity onto the horizontal components of seismometers. This causes sensitivity of these components to tilt, especially at low frequencies. We analyse the consequences of this effect onto moment tensor inversion for very long period (vlp) events in the near field of active volcanoes on the basis of synthetic examples using the station distribution of a real deployed seismic network and the topography of Mt. Merapi volcano (Java, Indonesia). The examples show that for periods in the vlp range of 10–30 s tilt can have a strong effect on the moment tensor inversion, although its effect on the horizontal seismograms is significant only for few stations. We show that tilts can be accurately computed using the spectral element method and include them in the Green's functions. The (simulated) tilts might be largely influenced by strain–tilt coupling (stc). However, due to the frequency dependence of the tilt contribution to the horizontal seismograms, only the largest tilt signals affect the source inversion in the vlp frequency range. As these are less sensitive to stc than the weaker signals, the effect of stc can likely be neglected in this application. In the converse argument, this is not necessarily true for longer periods, where the horizontal seismograms are dominated by the tilt signal and rotational sensors would be necessary to account for it. As these are not yet commercially available, this study underlines the necessity for the development of such instruments.

Key words: Earthquake source observations; Volcano seismology; Computational seismology; Wave propagation.

1 INTRODUCTION

Source inversion is an important concept in volcano seismology to understand the characteristics of the seismic signals recorded in terms of mechanism and time history of the seismic sources—which then are interpreted in a larger context to better understand the volcanic activity. The technique of source inversion has successfully been used on various volcanoes and by a number of research groups, where the majority of the studies focuses on periods longer than 1 s (e.g. Ohminato *et al.* 1998; Chouet *et al.* 2003; Davi *et al.* 2010). The velocity structure of most volcanic edifices is heterogeneous and insufficiently known, making it difficult to simulate accurate Green's functions especially for high frequencies (e.g. Lokmer *et al.* 2007; Bean *et al.* 2008; Métaxian *et al.* 2009), while for low frequencies homogeneous velocity models including the topography are accurate enough for estimating stable results (e.g. Davi *et al.* 2010, see also references in Table 1).

The effects of tilt on horizontal components of seismometers have been known since the advent of broad-band seismometry (Rodgers

1968) and have also been studied more recently for modern instruments and the most general input ground motions (e.g. Graizer & Kalkan 2008). However, there are many papers published on source inversions for very long period events (vlp) using periods longer than 10 s without taking tilt into account (compare Table 1 for a selection). Chouet *et al.* (2003) are aware of a possible tilt effect and put the inverted source into a forward simulation to show that the effect of tilt on the seismograms is small. The examples in this study show that the effect on the inversion can still be large, as the tilt effect is correlated on all stations (in contrast to random noise) and thus does not necessarily average out in the inversion.

Maeda *et al.* (2011) propose a method to account for the tilt sensitivity of horizontal seismometers in the moment tensor inversion and applied this to data recorded at Asama volcano, Japan (Maeda & Takeo 2011). For the required computation of tilt Green's functions they present a finite difference (FD) method. Topography is approximated with staircase sampling which causes large errors in the computation of spatial derivatives of the wavefield (e.g. Pelties *et al.* 2010). Maeda *et al.* (2011) reduce this error by averaging the tilt at five adjacent cells in the direction of tilt. As one modification we propose a simple method to include rotational output into high-order finite element methods and test this method

*Now at: Institute of Geophysics, ETH Zurich, Sonneggstrasse 5, 8092 Zurich, Switzerland.

Table 1. Seismic source inversion studies for vlp events.

Volcano	Country	Periods	No. of stations	References
Kilauea	Hawaii, USA	8–100 s	11	Ohminato *et al.* (1998)
Aso	Japan	10–30 s	13	Legrand *et al.* (2000)
Stromboli	Italy	2–30 s	13	Chouet *et al.* (2003)
Popocatépetl	Mexico	15–70 s	9	Chouet *et al.* (2005)
Stromboli	Italy	2–30 s	21	Chouet *et al.* (2008)
Erebus	Antarctica	5–30 s	6	Aster *et al.* (2008)
Ontake	Japan	20–80 s	14	Nakamichi *et al.* (2009)
Augustine	Alaska	10–30 s	5	Dawson *et al.* (2011)
Asama	Japan	5–30 s	14	Maeda & Takeo (2011)

using an analytical reference solution in a homogeneous half-space with tilted surface.

However, modelling the tilt Green's functions is subject to a more fundamental difficulty: given the inherent ignorance of the small-scale subsurface medium properties and topography, one has to use some average or 'homogenized' structure and smoothed surface topography to simulate wave propagation using numerical techniques. From the seminal argument by Backus (1962) as well as from more modern approaches to homogenization theory (e.g. Capdeville *et al.* 2010) it is well known that the elastic displacements and stresses are well approximated by their homogenized versions. In contrast, the gradient of the displacement which contains the strain and the rotation depends in first order on the medium properties (i.e. a discontinuity in the elastic parameters causes a discontinuity in the gradient) and is not necessarily well approximated by the homogenized fields. One problem anticipated for the numerical computation of tilt Green's functions is thus strain–rotation coupling (src) that could be present in the data due to small-scale inhomogeneities and topography that is not resolved by the numerical model. This effect transforms strains into local rotations which in most volcanic settings with rough topography and strong subsurface heterogeneity will be inevitable even with careful site selection. In a previous study (van Driel *et al.* 2012), we estimated the order of magnitude of the src constants to 0.1–0.3, which is in agreement with other studies (Harrison 1976; Wielandt & Forbriger 1999; Lambotte *et al.* 2006).

A complementary approach to cope with tilt-contaminated seismograms in the source inversion would be to measure the tilts *in situ* and correct the seismograms in post-processing. If all six degrees of freedom of a solid body (three components of translation and three of rotation) are recorded, it is in principle possible to recover its whole trajectory (e.g. Lin *et al.* 2010). Furthermore, the rotational seismograms would not only allow the correction of the horizontal seismograms for the tilt effect, but could also be used as additional complementary data and potentially enhance the source inversion using the same number of stations that need to be installed in the field (Bernauer *et al.* 2014). Unfortunately, field suitable rotational sensors with the necessary precision and reliability are not yet available (e.g. Nigbor *et al.* 2009; Wassermann *et al.* 2009; Bernauer *et al.* 2012). For now, including the tilt in the Green's function is thus the only way to account for tilt in moment tensor inversion of vlp events.

2 FORWARD SIMULATION OF ROTATIONAL MOTIONS

The first task in our tilt corrected source inversion lies in the forward computation of both translational and rotational motions. In order to simulate seismograms in a model including 3D topography, we use the spectral element method on unstructured hexahedral meshes (SPECFEM3D in the cartesian version, see Peter *et al.* (2011) and the references therein).

To measure the gradient of the wavefield, we place six additional stations around the real station that is used to record translation. Each of them is offset by 1 m in direction of one of the coordinate axes in positive or negative direction. The gradient is then computed using the central differences approximation and strain and rotation are found as the symmetric and antisymmetric part of the gradient.

2.1 Tilted surface test

The tests similar to those presented in Maeda *et al.* (2011) illustrate the strengths of this forward simulation method: the analytical solution of a static deformation observed at the free surface ($z = 0$), for an explosive source embedded in homogeneous half-space is (Okada 1992):

$$\text{vertical displ. :} \quad u_z = \frac{m_0}{4\pi\mu} \frac{z_0}{r^3} \tag{1}$$

$$\text{tilt :} \quad \theta_y = -\frac{\partial u_z}{\partial x} = \frac{3m_0}{4\pi\mu} \frac{z_0 x}{r^5}, \tag{2}$$

with source depth $z_0 = 500$ m, moment $m_0 = 10^{16}$ Nm, shear modulus $\mu = 4.95 \times 10^9$ Pa and distance to source r.

The computational domain consists of a cuboid of $10 \times 10 \times 4$ km^3 with an inclined surface ($10°$) on top (boundary conditions: free surface at the top and absorbing at the other surfaces). The model was meshed with hexahedrons of edge length 300 m in the volume and refined to 100 m at the surface, see Fig. 1(a), to have the same parameters as in the later simulations with topography. Within the elements the displacement is represented by degree-4 polynomials and is continuous at element boundaries. The gradient estimation is therefore fourth-order accurate and stable at element boundaries.

Fig. 1(b) shows the comparison of analytical and numerical results for the tilt as well as the absolute error. The tilt is the static tilt remaining after the seismic waves are attenuated at the absorbing boundaries after ≈50 s of simulation. The general trend of the error is a consequence of the finite domain in the numerical computation, the maximum error of the tilt is about 1.5 per cent of the maximum tilt. The main advantage of the spectral element method in comparison to the FD code used by Maeda *et al.* (2011) in this specific example is the ability to model the inclined surface exactly instead of using staircase sampling. We conclude that using this approach we can model dynamic tilt in smooth models to high accuracy, but recall the previously mentioned principal difficulty of computing
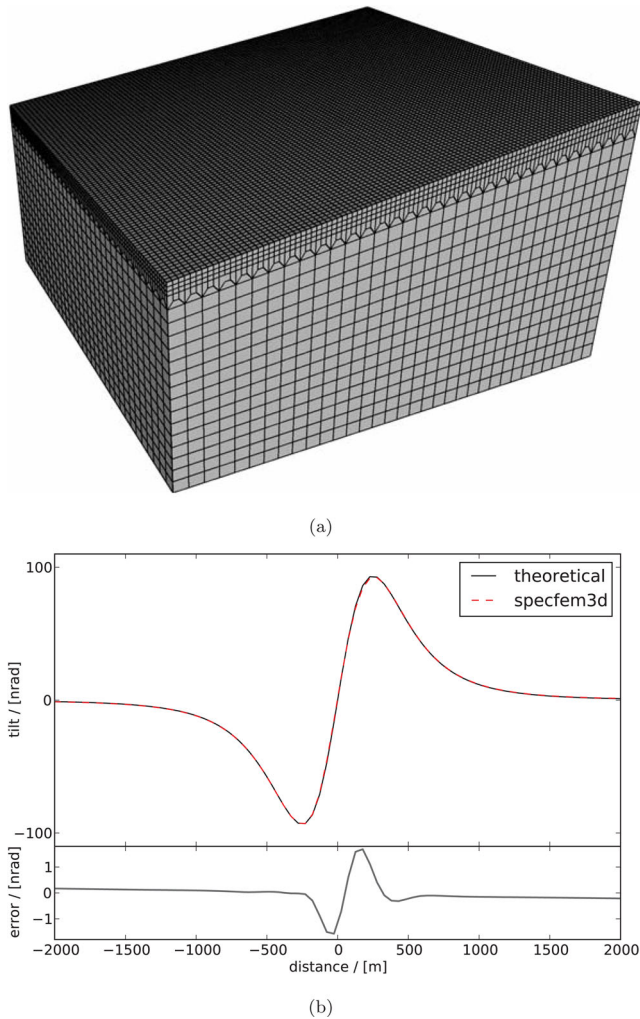
Figure 1. (a) Mesh with $10°$ inclined surface used for the simulation in (b). (b) Permanent tilt computed with SPECFEM3D compared to the analytical solution for an explosive source in homogeneous half-space in 500 m depth. Note the different scales on the *y*-axis for the absolute error.

the gradient of the wavefield in heterogeneous media with topography.

2.2 Strain–tilt coupling

For the synthetic examples we use a model of Mt. Merapi volcano (Java, Indonesia) and the station distribution of a real deployed seismic network (Wassermann & Ohrnberger 2001), see Fig. 2. The coverage of this network was not perfect, partly because the eastern flank of Merapi was inaccessible by the time of the field deployment. To improve it, we add eight fictitious stations (station codes ADA–ADH). In total, we use 20 stations, where three groups of three stations each are arranged as small aperture arrays (PAS, KLT and GRW). In comparison to the studies quoted in Table 1 we are at the upper limit in number of stations and argue that any study using less stations will likely experience stronger effects then we observe here. The topography model is based on a DEM model with 45-m resolution (Gerstenecker *et al.* 2005), which was smoothed by convolution with a 225 m kernel (Hanning window) for easier meshing with hexahedrons as required for SPECFEM3D. Though the smoothing will affect the actual waveforms (van Driel *et al.* 2012), we do not expect it to change the order of magnitude of the
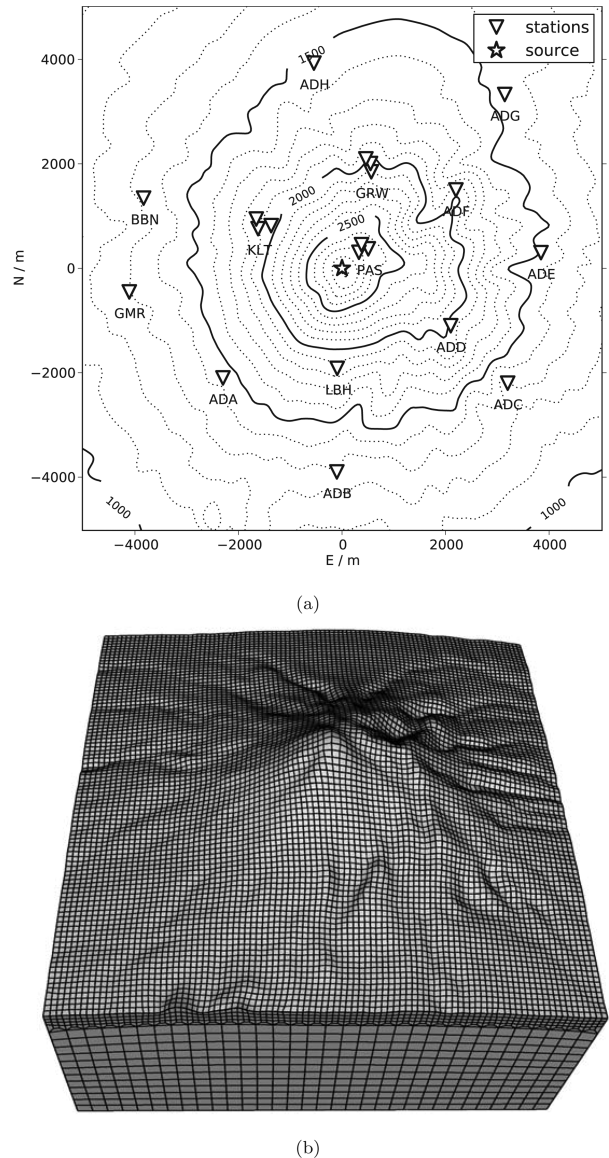

Figure 2. (a) Topography model, source location and the 12 stations used in the inversion. (b) Computational model.

tilt, which is most important for this study. The elastic parameters are chosen homogeneous in the whole volume with $\rho = 2200\,\mathrm{kg\,m^{-3}}$, $v_p = 3\,\mathrm{km\,s^{-1}}$ and $v_s = 1.5\,\mathrm{km\,s^{-1}}$. Any scattering that can be seen in the seismograms is hence due to the topography.

The computational domain consists of a cuboid of $10 \times 10 \times 3\,\mathrm{km^3}$ with the Mt. Merapi topography on top (free surface at the top and absorbing boundaries at the other surfaces). The model was meshed with hexahedrons of edge length 300 m inside the volume and refined to 100 m at the surface for better topography approximation. The point source is located at 2000 m height above sea level (asl) and vertically beneath the summit which is at 2970 m asl. We only consider moment tensor sources, so a total of six forward simulations (one for each independent moment tensor component) with Gaussian source time function (half duration 1 s) is sufficient to generate seismograms for arbitrary mechanisms by summation and convolution as in eq. (4) in the next section.

As only a smoothed version of the real topography and subsurface structure can be included in the model, strain-rotation
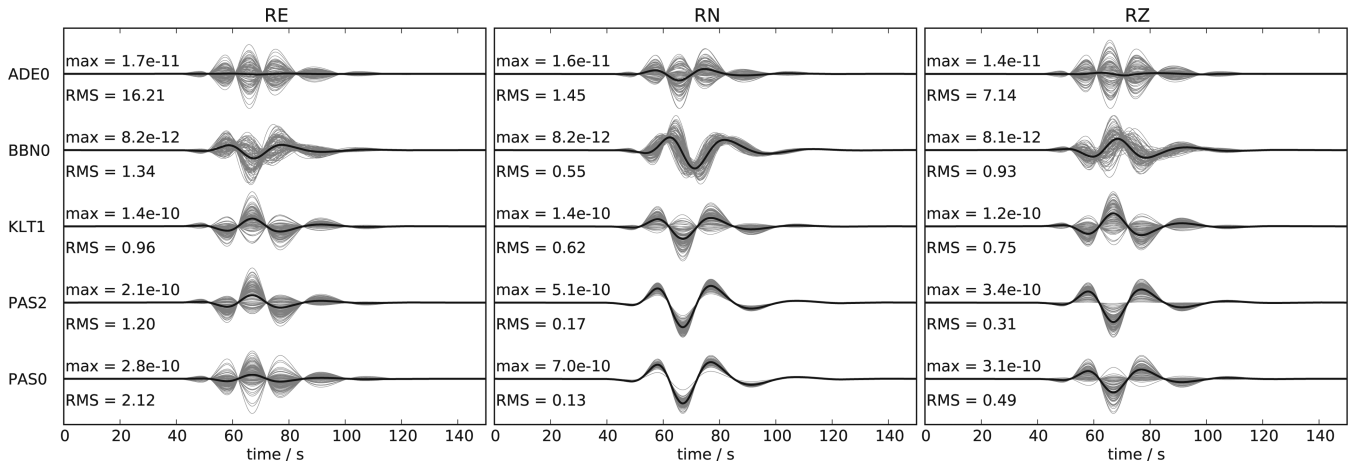
Figure 3. Normalized synthetic rotational seismograms for a vertical crack point source at Mt. Merapi. RN, RE and RZ denote rotation around the N, E and Z axes. Pure tilt signal (black) and 100 random realizations of strain–rotation coupling effect on the rotational seismograms (grey), numbers at each traces are maximum amplitudes in radians and rms errors averaged over the 100 traces.

coupling caused by inhomogeneities and small scale topography can cause differences between modelled and true rotational seismograms. Fig. 3 shows the normalized synthetic rotational seismograms, pure rotation as output of the simulation (black) and with additional strain-induced rotation (grey) for 100 realizations of random coupling constants: Based on the considerations in van Driel *et al.* (2012), all nine coupling constants are assumed to be normally distributed and the standard deviations are chosen $\sigma_\perp = \sigma_Z = \sigma_S = 0.2$ (for normal strain coupling into rotation perpendicular to the strain, for all strains coupling into rotation around the *z*-axis and for shear strain coupling into all three components of rotation respectively) and $\sigma_\parallel = 0.1$ (for parallel normal strain and rotation axes). For a quantitative measure we compute the mean of the rms of the single traces containing tilt-effect compared to the trace without tilt. The effect is larger than 10 per cent mean rms on all stations and dominating on some of them, for example, on the E-component of ADE0 where the translations are very small. The median of the mean rms over all horizontal rotations is 130 per cent. The reason for the varying order of magnitude of the effect on different stations is the difference in radiation patterns of strain and tilt and the interaction with the topography, such that the effect is strongest where tilts are small and strains are large.

3 THEORY

3.1 Moment tensor inversion in the frequency domain

Several authors have presented the basic theory for moment tensor inversion in great detail (e.g. Legrand *et al.* 2000; Aster *et al.* 2005; Cesca & Dahm 2008; Davi *et al.* 2010), therefore we restrict ourselves to a concise summary. In the synthetic examples of this study, we assume that the location of the source is known in order to concentrate on the effect of tilt on the inversion for the source mechanism. In a realistic scenario, the source location needs to be found in a preceding processing step. Alternatively, the inversion for the source mechanism could be repeated in a grid search for a large number of source locations, where afterwards one location is selected based on the misfit of the synthetic seismograms compared to the observation.

The displacement $u_n(\mathbf{x}, t)$ at location $\mathbf{x}$ for a point source at $\mathbf{x}^s$ can be written in the form (e.g. Aki & Richards 2002)

$$u_n(\mathbf{x}, t) = \sum_{pq} \frac{\partial G_{np}(\mathbf{x}, \mathbf{x}^s, t)}{\partial x_q^s} \star M_{pq}(t)$$
$$+ \sum_p G_{np}(\mathbf{x}, \mathbf{x}^s, t) \star F_p(t), \tag{3}$$

where $G_{np}(\mathbf{x}, \mathbf{x}^s, t)$ is the Green's function, $M_{pq}(t)$ and $F_p(t)$ are the source's moment tensor and single force and $\star$ denotes the convolution. The existence of a single force part in volcanic source was first suggested by Takei & Kumazawa (1994) and is still in debate (De Barros *et al.* 2013). Although we do not invert for the single force in our examples, we keep it in the theory section for completeness. Using the convention of summation over repeated indices, in the frequency domain this can be written as

$$u_n(\mathbf{x}, \omega) = \left(M_{pq}(\omega) \frac{\partial}{\partial x_q^s} + F_p(\omega) \right) G_{np}(\mathbf{x}, \mathbf{x}^s, \omega). \tag{4}$$

Assuming finite window length of the data and using the discrete Fourier transform, this can be written as a linear system of the form

$$\mathbf{u} = \mathbf{Gm}, \tag{5}$$

where $\mathbf{u}$ contains the data, $\mathbf{G}$ the Green's function and it's derivatives and $\mathbf{m}$ the moment tensor and single force components (see, e.g. Davi *et al.* (2010) for explicit form). In the frequency domain, $\mathbf{G}$ is block-diagonal where each block corresponds to one discrete frequency. Instead of one large matrix inversion, the problem can hence be split into the inversion of one smaller matrix for each frequency. The linear system in eq. (5) can be inverted for the source components by minimization of the residual

$$\varepsilon^2(\omega) = \frac{(\mathbf{u} - \mathbf{Gm}^{inv})^T \mathbf{W}^2 (\mathbf{u} - \mathbf{Gm}^{inv})}{\mathbf{u}^T \mathbf{W}^2 \mathbf{u}} \tag{6}$$

with the estimate (Menke 1989)

$$\mathbf{m}^{inv} = (\mathbf{G}^T \mathbf{W}^2 \mathbf{G})^{-1} \mathbf{G}^T \mathbf{W}^2 \mathbf{u}, \tag{7}$$

where $\mathbf{W}$ is a diagonal weighting matrix. We perform the inversion of the term in parentheses using a singular value decomposition (SVD). Though the inverse should be well defined by itself as it represents an overdetermined problem as long as enough stations

are used, we enforce stability additionally by using singular values only that are larger than 10^{-5} times the largest one.

For the weighting we choose one common weight for all three components j at each station i,

$$W_i^2 = \frac{1}{\sum_j \int |u_j(\mathbf{x}_i, t)|^2 \mathrm{d}t}. \tag{8}$$

Integrating the ε^2 in time domain over time and defining $\mathbf{u}^{\mathrm{inv}} = \mathbf{G}\mathbf{m}^{\mathrm{inv}}$ gives the misfit

$$\epsilon^2 = \int \varepsilon^2(t)\,\mathrm{d}t = \sum_i \frac{\sum_j \int |u_j(\mathbf{x}_i, t) - u_j^{\mathrm{inv}}(\mathbf{x}_i, t)|^2 \mathrm{d}t}{\sum_j \int |u_j(\mathbf{x}_i, t)|^2 \mathrm{d}t}. \tag{9}$$

The seismograms are thus weighted with the sum of the L2-norm of all three components in the inversion, as suggested by Chouet *et al.* (2003) and Ohminato *et al.* (1998) to deal with the large amplitude differences caused by varying distance to the source in the near field. It is important to note that the choice of the misfit measure is an implicit assumption about the noise present in the data: uncorrelated white Gaussian noise with same magnitude on all three components of the seismometers and with power ratios according to the station weighting coefficients. We will come back to this in the discussion of the Akaike Information Criterion (AIC) and the examples.

So far, the result is the moment tensor as a function of time. This is also referred to as 'unconstrained' inversion in the literature, as there is no further constraint on the source mechanism or the source time function to be the same on all moment tensor components. Consequently, the source mechanism is also time dependent. Using a second SVD, the time-dependent moment tensor can be decomposed into six mechanisms and corresponding source time functions (Vasco 1989; Cesca & Dahm 2008). The moment tensor can be constrained to a single mechanism by selecting the mechanism with the largest singular value (principal component analysis, pca). The ratio of the first to the other singular values is then an indication of how good the assumption of a single mechanism is.

3.2 Tilt effects on horizontal seismograms

In a series of papers, Graizer *et al.* study the response of various types of seismometers to general ground motions including rotations (Graizer 2005, 2006a,b, 2009, 2010; Graizer & Kalkan 2008) and Lin *et al.* (2010) show how to correct accelerometers for tilt effects using rotational sensors based on an approach from inertial navigation systems. The most important conclusion for the effects concerning this study is that excluding strong motions and keeping first-order terms only, most sensor types (mass-on-spring and mass-on-rod, also in Galperin configuration) behave similar and the only additional term is tilt (rotation around horizontal axes) on the horizontal components. For example, for a mass-on-spring type of pendulum, the full equation of motions for the horizontal pendulums is (Graizer & Kalkan 2008)

$$\underbrace{\ddot{x}_{1/2}^p + 2\omega_0 D_0 \dot{x}_{1/2}^p + \omega_0^2 x_{1/2}^p}_{\text{harmonic oscillator}}$$

$$= \underbrace{-\ddot{u}_{1/2}}_{\substack{\text{horizontal} \\ \text{acceleration}}} \pm \underbrace{g\alpha_{2/1}}_{\text{tilt}} \pm \underbrace{\ddot{u}_3\alpha_{2/1}}_{\substack{\text{crossaxis} \\ \text{sensitivity}}} + \underbrace{l_p\dot{\phi}^2}_{\substack{\text{centrifugal} \\ \text{acceleration}}}, \tag{10}$$

where $x_{1/2}^p$ is the displacement of the pendulum in the two horizontal perpendicular directions, ω_0 is the eigenfrequency, D_0 is the damping of the harmonic oscillator, $\alpha_{2/1}$ is the tilt around a horizontal axis, ϕ is the rotation around the vertical axis and l_p is the length

of the pendulum. The sign of $\alpha_{2/1}$ here is valid for a right-handed system where the third axis is vertical up and using the right-hand rule to define the direction of rotation. Omitting second-order terms and introducing the instrument response function $T(\omega)$ for displacement, eq. (10) can be represented in the frequency domain as

$$x_{1/2}^p(\omega) = T(\omega)\left(u_{1/2}(\omega) \pm \frac{g}{\omega^2}\alpha_{2/1}(\omega)\right). \tag{11}$$

Eq. (11) shows that the tilt effect is proportional to $1/\omega^2$, which is equivalent to the second time integral in time domain. It will thus be large for low frequencies and negligible for high frequencies, where 'high' and 'low' are to be determined for the specific problem as the relative amplitudes of $\alpha_{2/1}$ and $u_{1/2}$ can vary strongly depending on source parameters and thus radiation pattern and distance. It is important to note that the near field terms that do have a strong influence in the vlp events are proportional to the source time function (stf). Using a step function as the stf causes permanent tilt in the near field and thus strong effects in low frequencies. This is in contrast to the far field terms that are proportional to the derivative of the stf and more relevant in regional applications of moment tensor inversion, where no permanent tilt is expected (e.g. Shearer 2009; Lokmer & Bean 2010).

3.3 Including tilt in the Green's functions

In a recent paper Maeda *et al.* (2011) propose a method to include the tilt into the Green's functions to account for the tilt in the inversion. Our development in this section is mostly equivalent to their results. Using a slightly more rigorous notation, we want to show that the tilt effect can effectively be absorbed into what we will call 'apparent' Green's functions. Defining the term in parentheses in eq. (11) as the 'apparent' displacement (i.e. what seismometers are actually sensitive to in first order) and using eq. (4) as well as $\alpha_{1/2} = \pm\frac{1}{2}(\frac{\partial u_3}{\partial x_{2/1}} - \frac{\partial u_{2/1}}{\partial x_3})$ we can write

$$\begin{aligned}
\tilde{u}_{1/2} &= u_{1/2} - \frac{g}{2\omega^2}\left(\frac{\partial u_3}{\partial x_{1/2}} - \frac{\partial u_{1/2}}{\partial x_3}\right) \\
&= \left(M_{pq}\frac{\partial}{\partial x_q^s} + F_p\right)\left(G_{1/2p} - \frac{g}{2\omega^2}\left(\frac{\partial G_{3p}}{\partial x_{1/2}} - \frac{\partial G_{1/2p}}{\partial x_3}\right)\right) \\
&= \left(M_{pq}\frac{\partial}{\partial x_q^s} + F_p\right)\tilde{G}_{1/2p} \tag{12}
\end{aligned}$$

for the horizontal components. As tilt has no first order effect on the vertical component, this defines the apparent Green's function $\tilde{G}$. As eq. (12) has the same form as eq. (4), the inversion for the moment tensor M_{pq} can be done with the same algorithm as before, the only difference is in the Green's functions and seismograms. In principle any moment tensor inversion code available (e.g. VOLPIS, Cesca & Dahm (2008), ISOLA, Sokos & Zahradnik (2008), or the code by Ohminato *et al.* (1998)) could be used with the modified Green's functions including tilt.

However, there is one additional technical problem: As the focus of this study is on very long periods ($>10\,\mathrm{s}$), the stations are within one wavelength of the source, thus in the near field. The Green's functions are seismograms generated by an impulsive source and mainly have the same shape as the stf in the near field (e.g. Shearer 2009). The second time integral of the tilt hence contains a large linear term leading to a large step at the end of the time window which needs to be treated with special care. Maeda *et al.* (2011) suggest to convolve the Green's functions with the instrument response to get rid of the linear term and stabilize the convolution in

frequency domain by zeropadding. Alternatively, we can work with double differentiated waveforms and Green's functions, that do not contain the linear term. The advantage here is, that derivatives can be computed in time domain which avoids treating the step at the end of the time window in the Fourier transform. As taking the derivative is equivalent to multiplication by frequency on both sides of eq. (5) in frequency domain, this does not change the solution of the inverse problem.

3.4 Akaike's information criterion

Many previous authors use the statistical entropy based information criterion by Akaike (1974) to argue for the statistical significance of their source inversion results. Still, there is some skepticism about the validity of the AIC analysis in the community. Bean *et al.* (2008) and O'Brien *et al.* (2010) show that it may fail in the case of systematic errors for example caused from unknown velocity models. We suspect that additionally there is another common source for errors made when computing the AIC, that is the way of counting of *independent* degrees of freedom in the data.

The AIC in the form commonly used in the source inversion literature is defined as (e.g. Ohminato *et al.* 1998)

$$\text{AIC} = N_d \log \epsilon^2 + 2N_p, \tag{13}$$

where N_d is the number of independent data points, N_p the number of free parameters and ϵ^2 the squared error in the inversion as defined in eq. (9). Two solutions of the inverse problem with different parametrizations can then be compared and solutions with smaller AIC values are preferred. An increased N_p (i.e. a more detailed solution) then needs to be justified by a decrease of ϵ^2 (i.e. a better fit of the data) that depends on the number of degrees of freedom in the data N_d. Importantly, this form of the AIC is specific to the case of Gaussian errors in the data, which explains the observations by Bean *et al.* (2008) and O'Brien *et al.* (2010).

Many authors compute N_d based on the number of traces N_t times the number of samples N_s in the seismograms. The implicit assumption here is that all samples in the seismograms are uncorrelated, but the correlation length obviously depends on the sampling frequency and frequency content of the signal. In signal processing it has long been known, that a bandwidth-limited signal can be sampled alias-free and hence reconstructed exactly when it is sampled at the Nyquist rate (Nyquist 1928), which equals twice the bandwidth of the signal (if the lower limit of the bandwidth is zero, the Nyquist rate equals twice the highest frequency contained in the signal). An upper bound for the number of *independent* degrees of freedom that can be measured in the low pass filtered seismograms is thus determined by the length of the signal times the Nyquist rate. Given the typical sampling frequencies used on modern digital recording systems (>100 Hz) and the low signal frequencies recorded for vlp events (<1 Hz), this can easily cause a difference of a factor 100 in the estimation of N_d. If the number of temporal degrees of freedom in the source time function is not overestimated in the same way (e.g. by counting the number of spectral components in the inverted frequency range only or by using smooth elementary source time functions in the time domain) this leads to overestimation of the significance of reductions in the error ϵ^2 and consequently over-interpretation of the inverted source.

For the purpose of this paper, we actually do not need the absolute value of the AIC, but rather compare AIC values for different parametrizations of the source mechanism having the same number of degrees of freedom N_{df} in the source time function and each

seismogram according to the Nyquist rate. An easy way to avoid counting the number of temporal degrees of freedom then is to look at the relative values only and define $\text{AIC}_{rel} = \text{AIC}/N_{df}$. We used the AIC with estimation of temporal degrees of freedom according to the Nyquist rate in the analysis of Mt. Yasur field data (Kremers *et al.* 2013) and found this be a more conservative criterion compared to other published estimates. The AIC lead us to the conclusion that given the data recorded at Yasur, we could likely not resolve any source detail beyond an isotropic expansion.

4 SYNTHETIC TESTS

4.1 Example 1: random noise

In Fig. 4, we show an example of an inversion, where all assumptions from the inverse theory are fulfilled: the seismograms recorded at the 20 stations are computed by summation and convolution according to eq. (3) and using the same Green's functions as in the inversion. The point source is equivalent to a vertical crack opening in E-W direction with moment magnitude $M_w = 2.3$ ($M_{EE} = 3M_0$, $M_{NN} = M_0$, $M_{ZZ} = M_0$, $M_{NE} = 0$, $M_{NZ} = 0$, $M_{EZ} = 0$ and $M_0 = 1.27 \times 10^{12}$ Nm) and located 970 m vertically beneath the summit at 2000 m height asl. The noise is chosen to fulfill the assumptions made by the choice of the misfit: it is white noise with zero mean, uncorrelated on the different traces and with relative amplitudes according to the station weighting (the denominator in eq. 8). The absolute amplitudes are chosen such that after band-pass filtering between 10 s and 30 s and tapering the misfit between noise-contaminated and noise-free seismograms according to eq. (9) is $\epsilon^2 = 0.35$. The signals are shown in Fig. 4(a) and are scaled to their weight in the inversion, so that the amplitudes can directly be compared.

The inversion proves to be robust against the noise, Figs 4(b)–(e) show the result of the unconstrained inversion as well as the first two principal components. The first principal component mechanism agrees nicely with the input vertical crack and the AIC indicates, that a single mechanism is sufficient to explain the measurements and the 35 per cent of noise is not fitted. Also, the source time function is recovered with correct phase and amplitude and some additional noise. In essence, in this scenario correct interpretation of the source properties is likely.
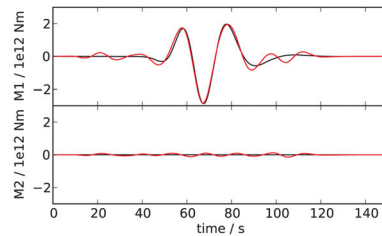
4.2 Example 2: tilt effect

In the second example, we calculate synthetics signals including the effect of dynamic tilt on the horizontal traces and invert these traces using tilt-free Green's functions. All other parameters are the same as in the previous example. Fig. 5(a) compares the undisturbed with the tilt-contaminated seismograms, showing that the effect is very small on most stations, zero for all vertical components and large for very few stations, in the example the E components of the station close to the summit (PAS). On average, the signal to noise ratio is a lot better in this example compared to the previous one with Gaussian noise, the tilt effect only causes a misfit $\epsilon^2 \approx 10$ per cent. The tilts-effect is of different nature then other types of noise as it is correlated on multiple stations and confined to the same time window as the translations. Usual processing techniques to remove or estimate noise will hence fail in the case of tilt.
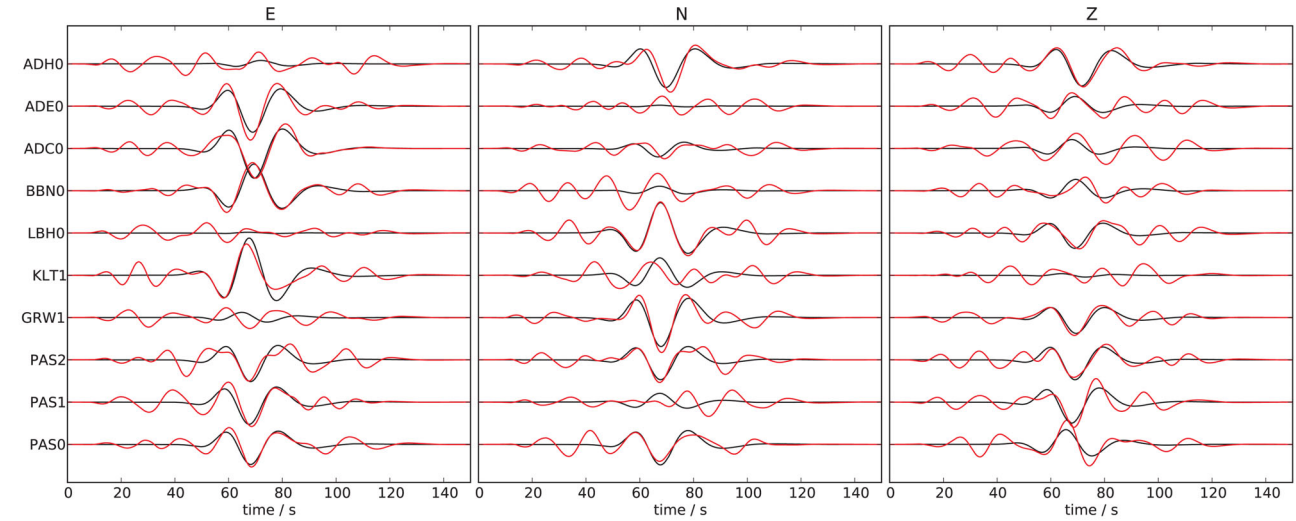
(a) black: translational seismograms of selected stations, red: seismograms with additional random noise, scaled to the L2-norm as used in the inversion
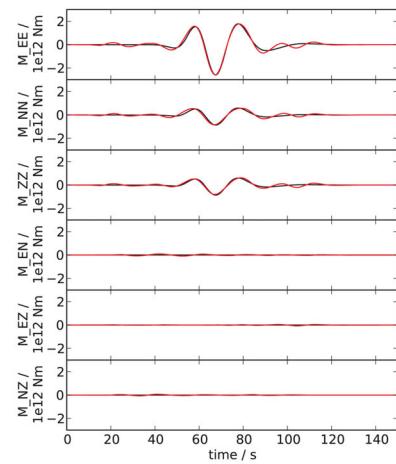

(b) black: input moment tensor, red: inversion result of the unconstrained inversion

(c) black: input moment tensor, red: inversion result, time dependence first and second principal component

(d) constrained inversion results allowing for 1-3 principal components: ratio of the singular values sv, misfit ϵ^2 and relative AIC

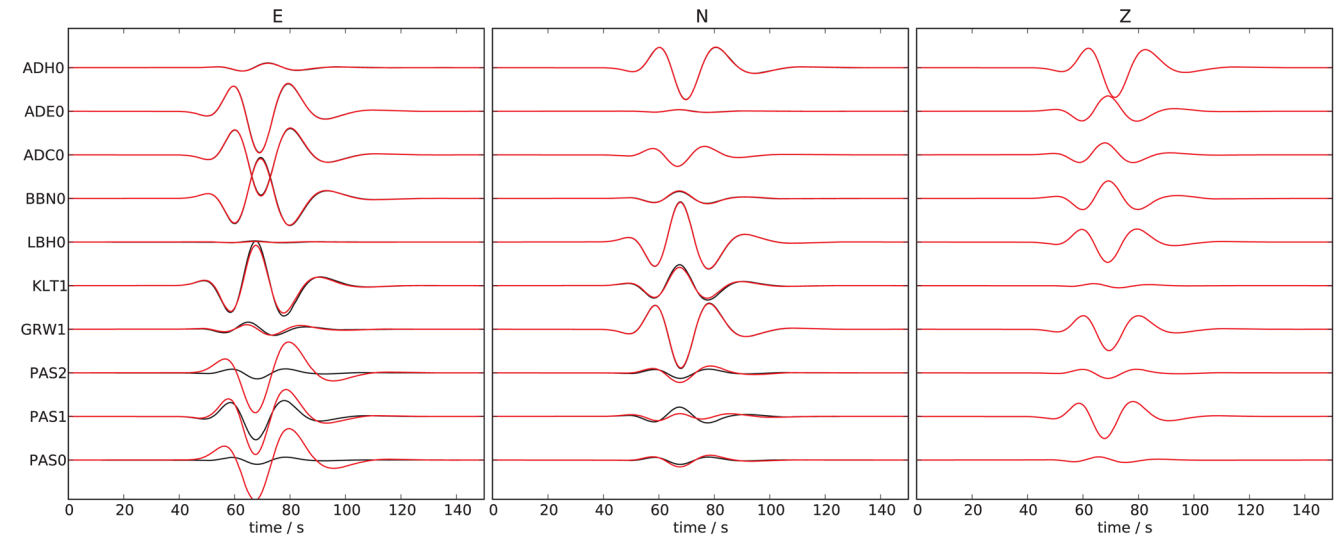| #pcs	1	2	3
$sv_i / \sum_k sv_k$	0.85	0.06	0.05
misfit	0.35	0.33	0.32
AIC_{rel}	-0.85	-0.70	-0.53
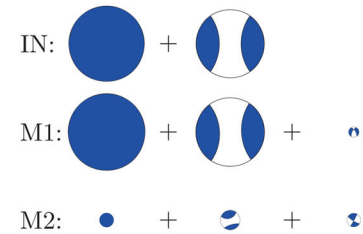
(e) graphic representation of input moment tensor and first two principal component mechanisms from the inversion decomposed into isotropic, CLVD and double couple contribution scaled to their magnitude

**Figure 4.** Example of moment tensor inversion with Gaussian noise.

The unconstrained inversion (Fig. 5b) shows more substantial differences compared to the true source than in the previous example, for example, M_{EZ} being nonzero. This is also visible in the principal component analysis (Figs 5c–e): The first principal component has an additional double couple component and the second principal component makes up for 23 per cent of the inverted moment although it is just an artefact. The relative AIC drop from -2.28 to -3.04 seems to indicate that this additional second moment tensor allows for significant improvement in fitting the data. So in conclusion, in this scenario correct interpretation of the result at least needs some caution, especially the AIC can be very misleading to be overly optimistic about the accuracy of the solution.

4.3 Example 3: strain tilt coupling

In the third example, we include the tilt-effect into the Green's functions and horizontal displacement seismograms (eq. 12). While we use the clean tilts from the numerical simulation for the Green's function, we additionally assume that the tilt on the seismograms is contaminated by strain-tilt coupling (Section 2.2). For a conservative estimate, we use random coupling constants two times larger then we estimated in a previous study (van Driel *et al.* 2012), i.e. normally distributed with $\sigma = 0.5$. While most of the rotational seismograms are heavily distorted by this effect as shown in Fig. 3, this is not the case for the tilt-contaminated horizontal translations in the period range $10-30$ s. Fig. 6 shows 100 realizations of

(a) black: translational seismograms of selected stations, red: seismograms with additional tilt effect on the horizontal components, scaled to the L2-norm as used in the inversion
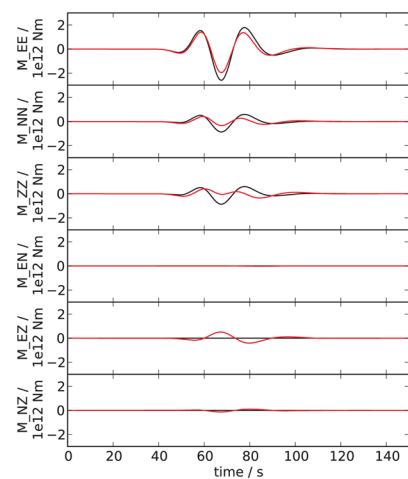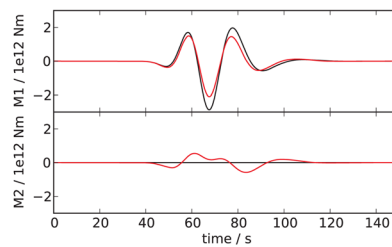
(b) black: input moment tensor, red: inversion result of the unconstrained inversion

(c) black: input moment tensor, red: inversion result, time dependence first and second principal component
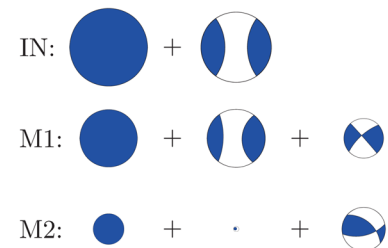
#pcs	1	2	3
$sv_i / \sum_k sv_k$	0.76	0.23	3.5e-3
misfit	0.084	0.032	0.032
AIC_{rel}	-2.28	-3.04	-2.84

(d) constrained inversion results allowing for 1-3 principal components: ratio of the singular values sv, misfit ϵ^2 and relative AIC

(e) graphic representation of input moment tensor and first two principal component mechanisms from the inversion decomposed into isotropic, CLVD and double couple contribution scaled to their magnitude

Figure 5. Example of moment tensor inversion with tilt-contaminated seismograms.

coupling coefficients and their effect on the translational seismograms including the tilt effect. The effect is significant and reaches average rms misfits up to 1.6 on the N component of PAS1, but it is a lot smaller then on the rotational seismograms. Importantly for the inversion, the traces with large relative amplitudes (i.e. after multiplying with the weighing according to eq. 8) are affected only up to 0.2 average rms because the contribution of tilt to the apparent displacement is small.

In contrast to the tilt-effect in example 2, which is correlated on all stations, the effect has a random sign, hence averages out in the inversion more easily. This assumption is crucial for generalization

of this result and might not be valid in all cases: the coupling coefficients are correlated on length scales similar to the correlation lengths of the medium, compare van Driel *et al.* (2012) Fig. 5 for an example with topography. Large scale structures found at many volcanoes like lava flows could possibly violate the assumption of randomness of the coupling constants.

We performed the same moment tensor inversion as above for random values of coupling constants that we consider realistic ($\sigma_\perp = \sigma_Z = \sigma_S = 0.2$) as well as for more extreme values ($\sigma = 0.5$). Without showing detailed results in the interest of brevity we just note that the recovered source fitted the input almost exactly in both
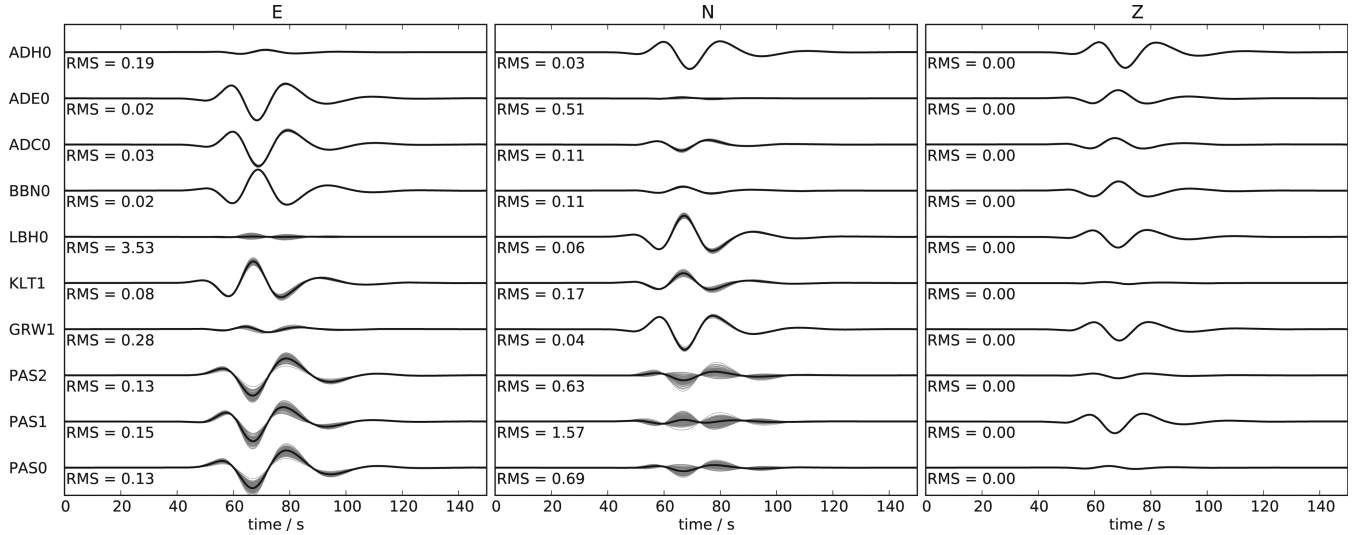
Figure 6. Translational seismograms including tilt effect for a vertical crack point source scaled to the L2 norm as used in the inversion. Unperturbed signal (black) and 100 random realizations of strain–rotation coupling effect on the rotational seismograms (grey) with very large values, so this can be considered an upper limit in the period range 10–30 s. The numbers at each traces are rms errors averaged over the 100 traces.

cases. Furthermore, we performed inversions using only a subset of 10 randomly selected stations, a number that is at the lower end among the studies collected in Table 1. Still, the strain-tilt coupling did not have significant influence on the inversion result.

4.4 Example 4: extremely long periods

For the previous three examples, we high-pass filtered the seismograms at 30 s, as this is what most previous studies used (compare Table 1). It is however clear from eq. (11) that the effect of tilt grows quadratically with the seismic period. Fig. 7 shows the amplitude fraction of the horizontal seismograms that originates from tilt γ, that is,

$$\gamma_{1/2}(\omega) = \frac{\left|\frac{g}{\omega^2}\alpha_{2/1}(\omega)\right|}{|u_{1/2}(\omega)| + \left|\frac{g}{\omega^2}\alpha_{2/1}(\omega)\right|} \tag{14}$$
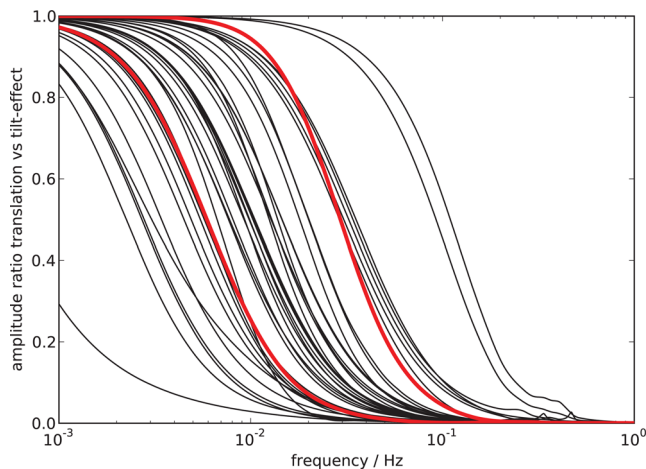

Figure 7. Amplitude fraction of the tilt contribution to the horizontal components for all 20 stations as a function of frequency, eq. (11). A value of 1 means that the trace is completely dominated by tilt, 0 means translation only. The red traces are from station GRW1 and are shown in time domain in Fig. 8.

with the tilts and translational motions generated by the same source as in the previous examples. As observed as well in example 2, in the frequency range 10–30 s there are two traces dominated by tilt (E component of PAS1 and PAS2) and five traces reach a value of 0.5 (i.e. half of the signal is caused by tilt) at the lower end of this frequency range (these correspond to the four remaining traces from the PAS stations and the E component of ADE0). In fact, only three of these contributed significantly to the inversion in example 2, due to the weighting to the sum of L2-norms of the three components. Moving to lower frequencies, below 100 s most traces are completely dominated by the tilt, even those where the tilt is relatively small and translation large. Fig. 8 visualizes the frequency dependence in time domain for the two horizontal traces of station GRW1 plotted in red in Fig. 7 by applying different filters.

The original argument for example 3 that only few traces are distorted by large tilt due to strain-tilt coupling is thus no longer valid. Now median rms errors of 130 per cent caused by strain-tilt coupling as we showed in Fig. 3 can in this case be expected for horizontal traces.

5 CONCLUSIONS

We showed, that tilt may have strong effects on the seismograms and on source inversions for periods longer than 10 s. The inversion can be affected strongly, even if the difference of the seismograms is quite small on most stations (17 out of 20 in our example). Still, the inverted source may reproduce the input seismograms nicely and the error is not necessarily recognized on the basis of the widely used error measures like the AIC. We tested the inversion method including tilt in the Green's functions proposed by Maeda *et al.* (2011) on several synthetic examples and find this procedure dramatically improves the inversion results for periods between 10–30 s – even if the Green's functions for tilt have some error due to strain-tilt coupling and even when only few stations are used, which is the case for many surveillance networks. This also means that tilt is not the dominating error anymore when included in the Greens functions, but all other sources of errors (noise, velocity model, topography, etc.) should still be considered for the network design.
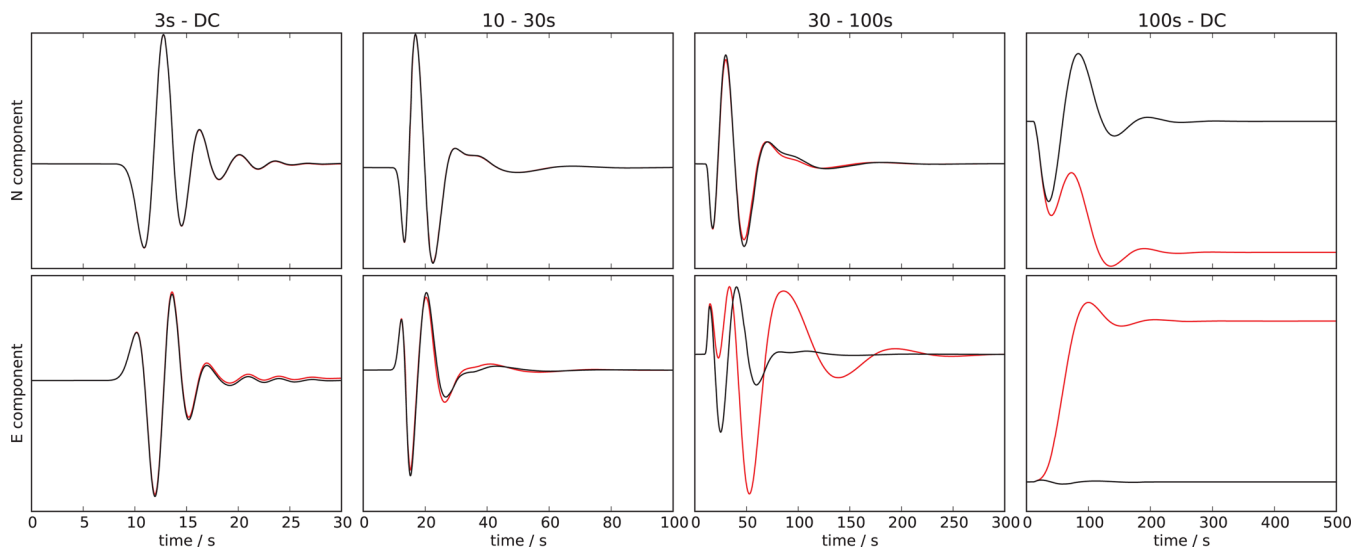
Figure 8. Normalized synthetic seismograms for a vertical crack point source with a Ricker wavelet as source time function and filtered to different passbands. Apparent permanent tilts originate from the double time integration of the tilt as it effects the horizontal components. The traces used in this plot are the N and E component of station GRW1 and are highlighted by red colour in Fig. 7.

These conclusions are so far based on theoretical considerations and simulations, which emphasizes the necessity of developing field suitable rotational sensors. These will be crucial to quantify the accuracy of synthetic rotational seismograms in the pronounced topography and heterogeneous subsurface typical for many volcanoes. Also, they will improve the source inversions of vlp events when used for tilt correction of horizontal seismograms, as this correction includes strain-tilt coupling in contrast to the synthetic tilt Green's functions and avoids the assumption of random distribution of coupling constants. Furthermore the rotational seismograms might be used as additional and complementary data to improve the inversion results using the number of stations in the field (Bernauer *et al.* 2014).

REFERENCES

Akaike, H., 1974. A new look at the statistical model identification, *Autom. Control. IEEE Trans.,* doi:10.1109/TAC.1974.1100705.

Aki, K. & Richards, P.G., 2002. *Quantitative seismology,* 2nd edn, Vol. 1, University Science Books.

Aster, R.C., Borchers, B. & Thurber, C.H., 2005. *Parameter Estimation and Inverse Problems,* Elsevier.

Aster, R., Zandomeneghi, D., Mah, S., McNamara, S., Henderson, D., Knox, H. & Jones, K., 2008. Moment tensor inversion of very long period seismic signals from Strombolian eruptions of Erebus Volcano, *J. Volc. Geotherm. Res.,* **177**(3), 635–647.

Backus, G., 1962. Long-wave elastic anisotropy produced by horizontal layering, *J. geophys. Res.,* **67**(11), 4427–4440.

Bean, C.J., Lokmer, I. & O'Brien, G.S., 2008. Influence of near-surface volcanic structure on long-period seismic signals and on moment tensor inversions: simulated examples from Mount Etna, *J. geophys. Res.,* **113**(B8), doi:10.1029/2007JB005468.

Bernauer, F., Wassermann, J. & Igel, H., 2012. Rotational sensors a comparison of different sensor types, *J. Seismol.,* **16**(4), 595–602.

Bernauer, M., Fichtner, A. & Igel, H., 2014. Reducing non-uniqueness in finite source inversion using rotational ground motions, *J. geophys. Res.,* **119**(6), 4860–4875.

Beyreuther, M., Barsch, R., Krischer, L., Megies, T., Behr, Y. & Wassermann, J., 2010. ObsPy: a Python toolbox for seismology, *Seismol. Res. Lett.,* **81**(3), 530–533.

Capdeville, Y., Guillot, L. & Marigo, J.-J., 2010. 1-D non-periodic homogenization for the seismic wave equation, *Geophys. J. Int.,* **181**(2), 897–910.

Cesca, S. & Dahm, T., 2008. A frequency domain inversion code to retrieve time-dependent parameters of very long period volcanic sources, *Comput. Geosci.,* **34**(3), 235–246.

Chouet, B.A. *et al.*, 2003. Source mechanisms of explosions at Stromboli Volcano, Italy, determined from moment-tensor inversions of very-long-period data, *J. geophys. Res.,* **108**(B1), ESE 7-1–ESE 7-25.

Chouet, B.A., Dawson, P. & Arciniega-Ceballos, A., 2005. Source mechanism of Vulcanian degassing at Popocatépetl Volcano, Mexico, determined from waveform inversions of very long period signals, *J. geophys. Res.,* **110**(B7), 1–20.

Chouet, B., Dawson, P. & Martini, M., 2008. Shallow-conduit dynamics at Stromboli Volcano, Italy, imaged from waveform inversions, *Geol. Soc. London, Spec. Publ.,* **307**(1), 57–84.

Davi, R., O'Brien, G.S., Lokmer, I., Bean, C.J., Lesage, P. & Mora, M., 2010. Moment tensor inversion of explosive long period events recorded on Arenal volcano, Costa Rica, constrained by synthetic tests, *J. Volc. Geotherm. Res.,* **194**(4), 189–200.

Dawson, P.B., Chouet, B.A. & Power, J., 2011. Determining the seismic source mechanism and location for an explosive eruption with limited observational data: Augustine Volcano, Alaska, *Geophys. Res. Lett.,* **38**(3), 1–5.

De Barros, L., Lokmer, I. & Bean, C.J., 2013. Origin of spurious single forces in the source mechanism of volcanic seismicity, *J. Volc. Geotherm. Res.,* **262,** 1–6.

Gerstenecker, C., Läufer, G., Steineck, D., Tiede, C. & Wrobel, B., 2005. Validation of digital elevation models around Merapi Volcano, Java, Indonesia, *Nat. Hazards Earth Syst. Sci.,* **5**(6), 863–876.

Graizer, V., 2005. Effect of tilt on strong motion data processing, *Soil Dyn. Earthq. Eng.,* **25**(3), 197–204.

Graizer, V., 2006a. Tilts in Strong Ground Motion, *Bull. seism. Soc. Am.,* **96**(6), 2090–2102.

Graizer, V., 2006b. Equation of pendulum motion including rotations and its implications to the strong-ground motion, in *Earthquake Source Asymmetry, Structural Media and Rotation Effects,* pp. 471–485, eds, Teisseyre, R., Majewski, E. & Takeo, M., Springer.

Graizer, V., 2009. The Response to Complex Ground Motions of Seismometers with Galperin Sensor Configuration, *Bull. seism. Soc. Am.,* **99**(2B), 1366–1377.

Graizer, V., 2010. Strong motion recordings and residual displacements: what are we actually recording in strong motion seismology?, *Seismol. Res. Lett.,* **81**(4), 635–639.

Graizer, V. & Kalkan, E., 2008. Response of pendulums to complex input ground motion, *Soil Dyn. Earthq. Eng.,* **28**(8), 621–631.

Harrison, J.C., 1976. Cavity and topographic effects in tilt and strain measurement, *J. geophys. Res.,* **81**(2), 319–328.

Kremers, S., Wassermann, J., Meier, K., Pelties, C., van Driel, M., Vasseur, J. & Hort, M., 2013. Inverting the source mechanism of Strombolian explosions at Mt. Yasur, Vanuatu, using a multi-parameter dataset, *J. Volc. Geotherm. Res.,* **262,** 104–122.

Lambotte, S., Rivera, L. & Hinderer, J., 2006. Vertical and horizontal seismometric observations of tides, *J. Geodyn.,* **41**(1–3), 39–58.

Legrand, D., Kaneshima, S. & Kawakatsu, H., 2000. Moment tensor analysis of near-field broadband waveforms observed at Aso Volcano, Japan, *J. Volc. Geotherm. Res.,* **101**(1–2), 155–169.

Lin, C.J., Huang, H.P., Liu, C.C. & Chiu, H.C., 2010. Application of rotational sensors to correcting rotation-induced effects on accelerometers, *Bull. seism. Soc. Am.,* **100**(2), 585–597.

Lokmer, I. & Bean, C.J., 2010. Properties of the near-field term and its effect on polarisation analysis and source locations of long-period (LP) and very-long-period (VLP) seismic events at volcanoes, *J. Volc. Geotherm. Res.,* **192**(1–2), 35–47.

Lokmer, I., Bean, C.J., Saccorotti, G. & Patanè, D., 2007. Moment-tensor inversion of LP events recorded on Etna in 2004 using constraints obtained from wave simulation tests, *Geophys. Res. Lett.,* **34**(22), 1–6.

Maeda, Y. & Takeo, M., 2011. Very-long-period pulses at Asama volcano, central Japan, inferred from dense seismic observations, *Geophys. J. Int.,* **185**(1), 265–282.

Maeda, Y., Takeo, M. & Ohminato, T., 2011. A waveform inversion including tilt: method and simple tests, *Geophys. J. Int.,* **184**(2), 907–918.

Megies, T., Beyreuther, M., Barsch, R., Krischer, L. & Wassermann, J., 2011. ObsPy—what can it do for data centers and observatories?, *Ann. Geophys.,* **54**(1), doi:10.4401/ag-4838.

Menke, W., 1989. *Geophysical Data Analysis: Discrete Inverse Theory,* revised edn, Academic Press.

Métaxian, J.P., O'Brien, G.S., Bean, C.J., Valette, B. & Mora, M., 2009. Locating volcano-seismic signals in the presence of rough topography: wave simulations on Arenal volcano, Costa Rica, *Geophys. J. Int.,* **179**(3), 1547–1557.

Nakamichi, H., Kumagai, H., Nakano, M., Okubo, M., Kimata, F., Ito, Y. & Obara, K., 2009. Source mechanism of a very-long-period event at Mt Ontake, central Japan: response of a hydrothermal system to magma intrusion beneath the summit, *J. Volc. Geotherm. Res.,* **187**(3–4), 167–177.

Nigbor, R.L., Evans, J.R. & Hutt, C.R., 2009. Laboratory and field testing of commercial rotational seismometers, *Bull. seism. Soc. Am.,* **99**(2B), 1215–1227.

Nyquist, H., 1928. Certain topics in telegraph transmission theory, *Trans. AIEE,* **47**, 617–644.

O'Brien, G.S., Lokmer, I. & Bean, C.J., 2010. Statistical selection of the "best" seismic source mechanisms from inversions of synthetic volcanic long-period events, *J. geophys. Res.,* **115**(B9), B09303, 10.1029/2009JB006958.

Ohminato, T., Chouet, B.A., Dawson, P. & Kedar, S., 1998. Waveform inversion of very long period impulsive signals associated with magmatic injection beneath Kilauea Volcano, Hawaii, *J. geophys. Res.,* **103**(B10), 23 839–23 862.

Okada, Y., 1992. Internal deformation due to shear and tensile faults in a half-space, *Bull. seism. Soc. Am.,* **82**(4), 1018–1040.

Pelties, C., Käser, M., Hermann, V. & Castro, C.E., 2010. Regular versus irregular meshing for complicated models and their effect on synthetic seismograms, *Geophys. J. Int.,* **183**(2), 1031–1051.

Peter, D. *et al.*, 2011. Forward and adjoint simulations of seismic wave propagation on fully unstructured hexahedral meshes, *Geophys. J. Int.,* **186**(2), 721–739.

Rodgers, P., 1968. The response of the horizontal pendulum seismometer to Rayleigh and Love waves, tilt, and free oscillations of the Earth, *Bull. seism. Soc. Am.,* **58**(5), 1385–1406.

Shearer, P., 2009. *Introduction to Seismology,* 2nd edn, Cambridge Univ. Press.

Sokos, E.N. & Zahradnik, J., 2008. ISOLA a Fortran code and a Matlab GUI to perform multiple-point source inversion of seismic data, *Comput. Geosci.,* **34**(8), 967–977.

Takei, Y. & Kumazawa, M., 1994. Why have the single force and torque been excluded from seismic source models?, *Geophys. J. Int.,* **118**(1), 20–30.

van Driel, M., Wassermann, J., Nader, M.-F., Schuberth, B.S.A. & Igel, H., 2012. Strain rotation coupling and its implications on the measurement of rotational ground motions, *J. Seismol.,* **16**(4), 657–668.

Vasco, D., 1989. Deriving source-time functions using principal component analysis, *Bull. seism. Soc. Am.,* **79**(3), 711–730.

Wassermann, J. & Ohrnberger, M., 2001. Automatic hypocenter determination of volcano induced seismic transients based on wavefield coherence an application to the 1998 eruption of Mt. Merapi, Indonesia, *J. Volc. Geotherm. Res.,* **110**(1–2), 57–77.

Wassermann, J., Lehndorfer, S., Igel, H. & Schreiber, U., 2009. Performance Test of a Commercial Rotational Motions Sensor, *Bull. seism. Soc. Am.,* **99**(2B), 1449–1456.

Wielandt, E. & Forbriger, T., 1999. Near-field seismic displacement and tilt associated with the explosive activity of Stromboli, *Ann. Geofis.,* **42**(3), 407–416.